

# Dark Photon Oscillations in Waveguide

Yu-Xin Tian,<sup>1,\*</sup> Wenyu Wang,<sup>1,†</sup> Wen-Na Yang,<sup>2,‡</sup> and Bin Zhu<sup>3,§</sup>

<sup>1</sup>*Beijing University of Technology, 100124, Beijing, China*

<sup>2</sup>*Department of Physics and Institute of Theoretical Physics,  
Nanjing Normal University, Nanjing, 210023, China*

<sup>3</sup>*School of Physics, Yantai University, Yantai, 264005, China*

Dark photons, which can kinetically mix with ordinary photons, represent the simplest extension to the standard model. Detecting their oscillations with visible photons could provide crucial insights into the nature of dark matter and fundamental interactions beyond the standard model. We propose a novel laboratory-based approach to detect dark photon oscillations using a laser in an Optical Time-domain Reflectometry (OTDR) setup. The laser light propagating through the optical fiber undergoes oscillations with the dark photon, leading to measurable changes in the power flow. These oscillations can be precisely measured, leveraging its high sensitivity and efficiency in detecting small variations in the optical signal. This approach could provide a new avenue for probing dark photon oscillations in the laboratory and greatly improve the current experimental sensitivity to dark photon in a wide mass range.

## INTRODUCTION

Dark matter (DM) is a cornerstone of modern physics, confirmed by cosmological and astrophysical observations [1–4]. Among DM candidates, ultralight dark photons [5–8], denoted  $A'$ , stand out as particularly compelling. A dark photon (DP) is a hypothetical vector boson associated with a  $U(1)$  gauge symmetry in a hidden sector. It can serve as a dark matter candidate if it is stable and abundant from the early universe processes, such as through inflationary fluctuations [9–19], parametric resonances [20–26], the decay of cosmic strings [27] or misalignment mechanisms [28–32]. Ultralight masses, spanning  $10^{-22}$  to  $10^{-1}$  eV, enable wave-like behavior, addressing astrophysics' small-scale structure issues [33–35]. Moreover, dark photons can kinetically mix with ordinary photons,  $\gamma$ , through a renormalizable interaction  $\varepsilon F^{\mu\nu} F'_{\mu\nu}$  [5] that naturally arises from the blending of the two  $U(1)$  gauge fields. This mixing leads to oscillations between photons and dark photons, similar to neutrino oscillations, providing a promising new avenue for detection.

Dark photons are typically probed through their conversion to visible photons, producing a resonant signal in detectors. This assumes DPs are present in the laboratory, either as ambient dark matter or as emissions from the Sun. Existing methods for DPs include halo-scope experiments like TOKYO [36–39], FUNK [40], DM pathfinder and Dark E-field [41, 42], SHUKET [43], WIS-PDMX [44], SQuAD [45], light shining through walls [46–49], plasma telescopes [48, 50], Dark E-field [42], DM-Radio [51–54], MADMAX [55], CMB spectrum distortions [29, 56–58], and radio observations of solar emissions [59, 60].

In contrast, our method does not rely on the assumption that DPs constitute the dark-matter component: even if they serve merely as virtual particles predicted by new physics, they remain directly testable within our

framework. In this Letter, we propose a laboratory-scale approach to detect DPs using a waveguide (optical fiber) setup. The core mechanism involves the oscillation between DPs and visible photons, driven by an effective mass term in specific environments.

This effective mass naturally emerges in waveguides as distinct propagation modes, or in cavities as resonant modes. Unlike a cavity, where a single photon is measured and enhanced by the dissipation rate or quality factor  $Q$ , oscillations in waveguides occur during photon propagation. In the absence of DP-photon mixing, photon propagation is analogous to an overdamped harmonic oscillator: its intensity decays exponentially with distance  $P \sim P_0 \exp(-\beta z)$  [61, 62]. When mixing is present, however, the system behaves like an underdamped oscillator, exhibiting spatial oscillations in the photon power. In this regime, the signal can drop to zero and subsequently revive to a smaller amplitude - a smoking gun of oscillation  $P \sim P_0 \exp(-\beta z) \cos(\Delta k z)$ . By searching for this underdamped behavior, we gain direct sensitivity to DP.

Varying the radius of the optical fiber can tune the propagation modes to have resonant mixing with the DP, giving us a scan method. Then the smoking gun can be detected by measuring the power flow in Optical Time-domain reflectometry (OTDR). [63, 64] By comparing the observed spatial variation of the fitted Lorentzian amplitude to its statistical uncertainty in each resolution bin, this approach can achieve up to five orders of magnitude improvement in  $\varepsilon$  over existing methods, thereby offering a powerful and complementary means to explore dark-photon parameter space alongside cosmological searches.

## DARK PHOTON PROPAGATION AND OSCILLATION

Dark photons, hypothetical particles from a dark  $U(1)$  gauge theory, couple to visible photons via kinetic mixing, described by the Lagrangian

$$\mathcal{L} = -\frac{1}{4}F'_{\mu\nu}F'^{\mu\nu} - \frac{1}{2}m_{A'}^2 A'_\mu A'^\mu - \frac{\varepsilon}{2}F'_{\mu\nu}F^{\mu\nu}, \quad (1)$$

where  $\varepsilon \ll 1$  is the mixing parameter,  $m_{A'}$  is the dark photon mass,  $F'_{\mu\nu} = \partial_\mu A'_\nu - \partial_\nu A'_\mu$  is the dark photon field strength and  $F_{\mu\nu}$  is the visible photon field strength. This kinetic mixing enables oscillations between visible and dark photons when their effective masses align.

In waveguides, such as hollow metallic cylinders or optical fibers, electromagnetic waves are transversely confined, supporting only discrete transverse modes (TE or TM) with cutoff frequencies  $\omega_\xi$ . Frequencies below this cutoff do not propagate, behaving like massive photons with effective mass  $m_\xi = \omega_\xi$ , yielding  $k_z^2 = \omega^2 - m_\xi^2$ . Unlike cavities, where standing waves lack axial propagation, waveguides support traveling waves, enabling oscillations over distance, a feature absent in cavity-based systems. The coupled wave equations are

$$\left[ -\frac{\partial^2}{\partial t^2} + \frac{\partial^2}{\partial z^2} - \begin{pmatrix} m_\xi^2 & -\varepsilon m_{A'}^2 \\ -\varepsilon m_{A'}^2 & m_{A'}^2 \end{pmatrix} \right] \begin{pmatrix} A \\ A' \end{pmatrix} = 0. \quad (2)$$

The inclusion of the  $\partial^2/\partial z^2$  term enables oscillatory behavior along the  $z$ -axis. The off-diagonal terms, proportional to  $\varepsilon m_{A'}^2$ , mix the fields. Diagonalizing the mass matrix via a rotation  $B_1 = \cos\theta A - \sin\theta A'$ ,  $B_2 = \sin\theta A + \cos\theta A'$ , with  $\tan 2\theta = 2\varepsilon m_{A'}^2/(m_{A'}^2 - m_\xi^2)$ , yields resonant mixing when  $m_\xi \approx m_{A'}$ , driving power oscillations along the waveguide.

At the input end ( $z = 0$ ) of waveguide, a pure visible photon state ( $A'(0) = 0$ ) sets  $B_1(0) = \cos\theta A(0)$  and  $B_2(0) = \sin\theta A(0)$ . Each eigenstate evolves as  $B_i(z) = B_i(0)e^{i(k_{z,i}z - \omega t)}$ , and the visible field at the distance  $z$  is  $A(z) = \cos\theta B_1(z) + \sin\theta B_2(z)$ . The power  $P(z)$  includes an interference term  $\propto \cos[(k_{z,1} - k_{z,2})z]$ , given by

$$P(z) = P_0 e^{-2\beta z} [\eta_1^2 + \eta_2^2 + 2\eta_1\eta_2 \cos(\Delta k_z z)]. \quad (3)$$

with  $\eta_1, \eta_2$  are the ratios of the corresponding eigenstates. At resonance ( $m_\xi = m_{A'}$ ), maximal mixing occurs ( $\eta_1 = \eta_2 = 0.5$ ), yielding  $P(z) \propto [1 + \cos(\Delta k_z z)]/2$  (up to damping).

The top panel of Fig. 1 shows the group velocity of the propagation modes of a waveguide. In case of the input frequency near the resonance, the phase difference  $\Delta k_z z$  caused by the two orthogonal modes will become significant. This will be a different phenomenon from the multimode propagation in the waveguide or fiber in which the power flow will be constant for a monochromatic wave input. The oscillation happens in case of the

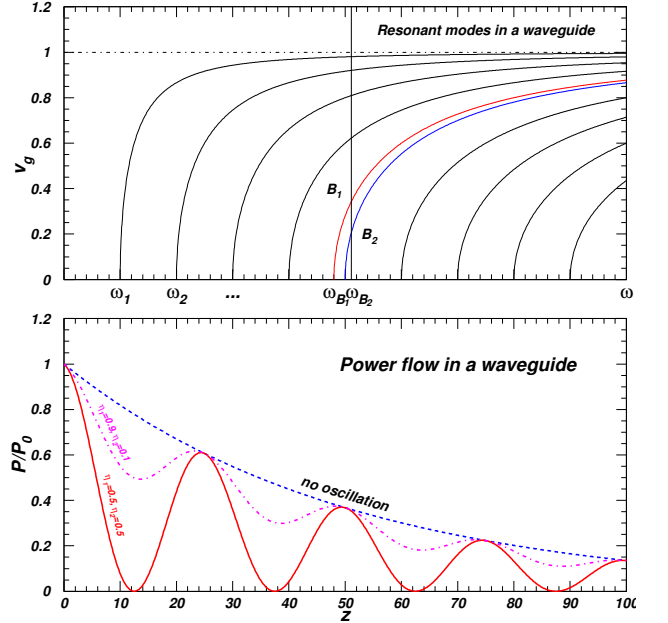


Figure 1. Dark photon oscillation. Top panel: sketch of the propagation modes in a waveguide.  $v_g$  is the group velocity. The red and blue curves show the resonant modes by the mixing between one mode and dark photon. Two different cut off frequency  $\omega_{B_1}, \omega_{B_2}$  are got after the diagonalization. The vertical line is the input frequency for the scan in the proposed measurement. Bottom panel: Power flow (normalized by  $P_0$ ) along the ( $z$ ) axle. Blue dash curve shows the attenuation without oscillation, Magenta dot dash line shows the attenuation with oscillation when  $\eta_1 = 0.9, \eta_2 = 0.1$ . Red solid curve shows the attenuation with oscillation at the resonance,  $\eta_1 = 0.5, \eta_2 = 0.5$ .

mixing with the dark photon, as for that only the visible photon can be detected in the lab. As shown in bottom panel of Fig. 1, the blue curve depicts the conventional photon intensity in the waveguide, exhibiting a purely exponential decay characteristic of an overdamped oscillator. Once photon–dark-photon mixing is introduced, energy is periodically exchanged between the two states, producing the underdamped oscillations illustrated by the red and purple curves. In this regime, the photon power falls to zero at the nodes of the oscillation and is subsequently restored to its peak value at the antinodes. The oscillation amplitude grows with the mixing parameter, becoming significant at maximal mixing,  $\eta = 0.5$ , where the revival of the photon signal is sufficiently large to enable detection of the dark photon.

In contrast to detection schemes that rely on ambient or solar-sourced dark photons, our waveguide-based setup induces photon–dark-photon mixing in a controlled laboratory environment—akin to reactor neutrino production—so that no preexisting dark-photon population is required. Consequently, there is no need for the dark photon to occupy a coherent state in the initial configuration, a crucial relaxation of the usual as-

sumption. Nearly all existing searches presuppose a coherent-state dark photon background to render the conversion signal detectable, yet the coherence of any dark-photon field remains unverified and may therefore challenge the viability of such approaches. By circumventing the coherent-state requirement, our method offers a model-independent pathway to probe dark photons on a tabletop experiment.

### EXPECTED SENSITIVITY

We propose to detect oscillations of visible photons into dark-photon states during propagation in an opti-

cal fiber, The fibers are ideal distributed sensors: they span kilometers, can be embedded readily within structures, are immune to electromagnetic interference, and allow each short segment to act as an independent sensing node. [65] When the effective mass of a guided mode matches the DP mass, resonant mixing splits the propagation eigenstates with distinct phase velocities. Interference between these eigenstates therefore produces a spatially oscillating power flow-rather than the usual monotonic attenuation-along the guide. OTDR, which measures position-resolved backscatter over long distances, is a natural and sensitive technique to detect the resulting cosine-like modulation of normalized power versus propagation length.

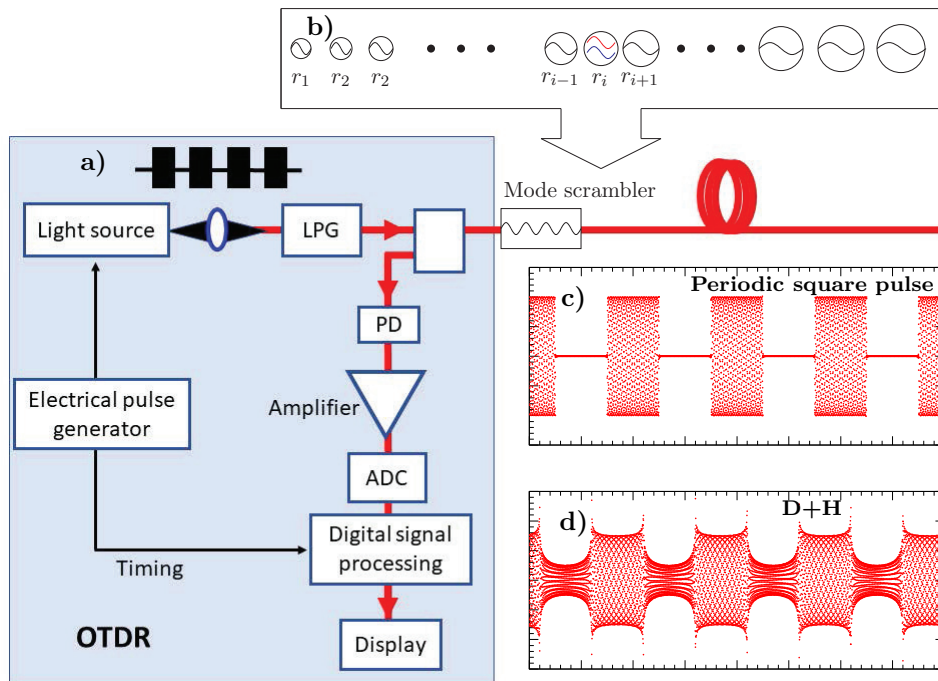


Figure 2. The sketch map of the experimental setup for measuring the oscillation of DPs by OTDR.

Fig. 2 presents the proposed OTDR-based measurement: [66]

- Panel a): the experimental layout.

A periodic optical pulse from a laser diode, driven by an electrical pulse generator, is launched into the test waveguide. A long-period grating (LPG) selects the guided mode of interest; an optional mode scrambler stabilizes the modal power distribution and suppresses cladding modes. Backscattered light is routed via a directional coupler to a photodiode (PD), amplified, and digitized

by an analog-to-digital converter (ADC); digitized traces are processed in a DSP that is synchronized to the source pulses so that the propagation delay of each backscattered feature is determined precisely.

- Panel b): resonant-mode scan.

The simplest way to scan the propagation modes is to prepare optical fibers with increasing radii and measure the corresponding power flow. The oscillation behavior appears when the effective guided-mode (cut off frequency) mass lies near the dark-photon mass  $m_{A'}$ . Also

the input frequency of laser should be tuned near the cut off frequency, too.

- Panel c): input squared pulse; Panel d): observed signature.

The illustrative square pulse (shown in panel c)) is a carrier at  $\omega_0$  modulated by a slow envelope  $\Omega \ll \omega_0$  and decomposes into the dominant tone  $\omega_0$ , lower harmonics  $\{\omega_0 - n\Omega\}$ , and higher harmonics  $\{\omega_0 + n\Omega\}$ . This decomposition motivates the ‘‘D+H’’ strategy: when  $\omega_0$  is tuned near the resonant mode the lower harmonics become evanescent and are filtered out by the guide, leaving the dominant tone plus higher harmonics (shown in panel d)) as the effective launched field. Note that there are some distortions of the waveform after a long propagation in the fiber, which will be shown in the supplemental material. Each spectral component propagates with phase velocity  $v_{p,B_i}^n = (\omega_0 + n\Omega)/k_{z,B_i}$ . So the two eigenstates accumulate a component-dependent phase difference

$$\Delta\varphi_n = L \left( \sqrt{(\omega_0 + n\Omega)^2 - m_{B_1}^2} - \sqrt{(\omega_0 + n\Omega)^2 - m_{B_2}^2} \right), \quad (4)$$

Finite laser coherence (fractional linewidth  $\zeta = \Delta\nu/\nu$ ) broadens the source and reduces the averaged phase difference. Modeling each spectral component with a Lorentzian lineshape  $g(\omega, \omega_c)$  leads to an averaged phase

$$\overline{\Delta\varphi_0} = \frac{4\varepsilon L}{\lambda} \int_0^\infty \frac{1}{\sqrt{x\zeta + 2\varepsilon} + \sqrt{x\zeta}} \frac{1}{1+x^2} dx, \quad (5)$$

Physically, finite  $\zeta$  partially washes out the phase accumulated by the carrier and thus imposes a lower bound on the observable  $\overline{\Delta\varphi_0}$ .

In all, the sensitivity in the OTDR is set by the fit uncertainty per measurement point, the coherence (linewidth) of the laser, and the effective baseline  $L_{\text{eff}}$ : long, coherent fibers and narrow laser linewidths increase accumulated phase difference and hence reach, whereas finite coherence and practical noise set the achievable limit on the kinetic-mixing parameter. This approach therefore converts distributed, laboratory-scale optical sensing into a quantitative bound on dark-photon mixing without accessing the fiber interior or using auxiliary fields, while requiring only standard fiber-optic instrumentation and mode control. In the experiment, we can measure backscatter-derived power  $\hat{P}(z_i)$  at a set of lengths  $\mathcal{M} = \hat{P}(z_1), \dots, \hat{P}(z_n)$ . Then we can compute normalized values  $P(z_i) = \hat{P}(z_i)e^{2\beta_\xi z_i}$  where  $\beta_\xi$  is the measured attenuation coefficient, which removes monotonic loss so that residual spatial structure reveals oscillation. Fit  $P(z)$  to a cosine model (or sinusoidal envelope appropriate to the two-eigenstate interference). A significant cosine component with the expected spatial period is evidence for oscillation. When  $\lambda_{\text{osc}} \gg L$  expand the cosine and use three-point measurements  $P(0), P(L/2), P(L)$  to estimate  $\Delta k_z L$  via newly defined

quantity  $\mathcal{E}(L)$

$$\mathcal{E}(L) = \frac{P(L/2) - P(0)}{P(L) - P(0)} \simeq \frac{1}{4} \left[ 1 + \frac{1}{16} (\Delta k_z L)^2 \right], \quad (6)$$

which yields  $\Delta k_z L \equiv \overline{\Delta\varphi_0}$ . Generally,  $\mathcal{E}(L)$  can be measured much more precisely with current fiber technology. For example, the limits in Fig. 3 are set by  $(\mathcal{E} - 0.25) \times 100 \simeq 0.006$ . Smaller values of  $\mathcal{E}(L)$  lead to stronger constraints on  $\varepsilon$ .

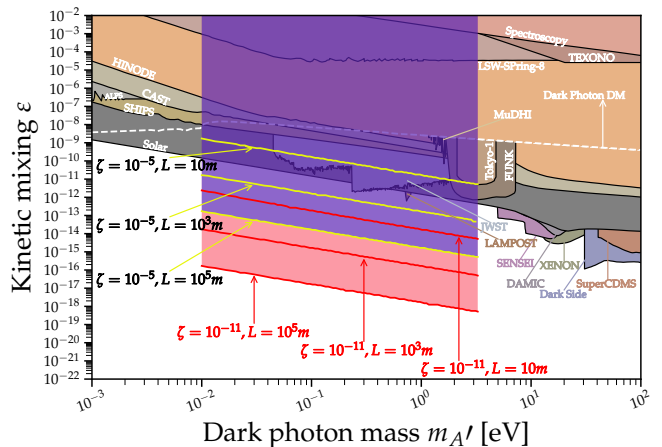


Figure 3. Expected sensitivity of the OTDR to dark photons. The frequency of the scan is chosen around that of infrared light  $0.8\mu\text{m} - 1.7\mu\text{m}$  used for telecommunication. [67]  $\zeta$  is chosen as  $10^{-5}$ ,  $10^{-11}$  for ordinary laser (yellow lines) and well controlled ultra-stable laser (red lines), respectively. [68] And the lengths of the optical fiber are set as 10m,  $10^3$ m, and  $10^5$ m. Other limits are got from Ref. [49]

As shown in Fig. 3, numerical results indicate that for common diode or telecom lasers with  $\zeta = 10^{-5}$ , even a 10 m optical fiber can set constraints comparable to the current solar global limit. Extending the baseline to 1 km improves the sensitivity by approximately an order of magnitude. Notably, for frequency-stabilized sources with  $\zeta = 10^{-11}$ , we find that the exclusion limits are enhanced by up to  $\mathcal{O}(7)$  orders of magnitude across the considered infrared wavelength range ( $0.8-1.7\mu\text{m}$ ), significantly surpassing existing experimental bounds. These results demonstrate that our method opens a new avenue for probing dark photons in previously inaccessible parameter regimes. Fully exploiting this potential requires a trade-off between increasing the baseline  $L$  and improving the source coherence.

## CONCLUSIONS

We have proposed a resonant, waveguide-based search for oscillations between visible photons and dark photons and shown that standard optical components—long-

period gratings for mode selection, mode scramblers, synchronized OTDR, and DSP—readily convert a tiny kinetic mixing into a macroscopic, position-dependent signature. It can improve sensitivity by many orders of magnitude over the current probe. The proposal is conceptually simple, experimentally tractable, and complementary to existing cavity, haloscope, and light-shining-through-wall searches: it probes a kinematic oscillation phenomenon that redistributes power between visible and invisible sectors rather than relying on ambient dark-photon flux. Practical challenges—mode-resolution in fabricated fibers, laser coherence, and enhanced attenuation near cutoff—are identified and mitigations are provided.

### ACKNOWLEDGEMENT

We would like to thank Lei Wu, Xiao-Hui Fang, Yun-Xin Wang, Qi-Wei Liang, Ji-Heng Guo and Yu-Song Cao for useful discussions. This work is supported by the NSFC under Grants No. 12475104, No. 12275232, No. 12335005, and No. 12275134.

---

\* tianyx2024@emails.bjut.edu.cn

† wywang@bjut.edu.cn

‡ yangwenna22@mails.ucas.ac.cn

§ zhubin@mail.nankai.edu.cn

- [1] V. C. Rubin and J. Ford, W. K., *Astrophys. J.* **159**, 379 (1970).
- [2] P. A. R. Ade *et al.* (Planck), *JCAP* **05**, 069 (2018), [arXiv:1502.01589 \[hep-ph\]](#).
- [3] L. Anderson *et al.* (BOSS), *Mon. Not. R. Astron. Soc.* **441**, 24 (2014), [arXiv:1312.4877 \[astro-ph.CO\]](#).
- [4] M. Tegmark *et al.* (SDSS), *Astrophys. J.* **606**, 702 (2004), [arXiv:astro-ph/0310725](#).
- [5] B. Holdom, *Phys. Lett.* **166B**, 196 (1986).
- [6] K. R. Dienes, C. F. Kolda, and J. March-Russell, *Nucl. Phys. B* **492**, 104 (1997), [arXiv:hep-ph/9610479](#).
- [7] S. A. Abel and B. W. Schofield, *Nucl. Phys. B* **685**, 150 (2004), [arXiv:hep-th/0311051](#).
- [8] S. A. Abel, J. Jaeckel, V. V. Khoze, and A. Ringwald, *Phys. Lett. B* **666**, 66 (2008), [arXiv:hep-ph/0608248](#).
- [9] P. W. Graham, J. Mardon, and S. Rajendran, *Phys. Rev. D* **93**, 103520 (2016), [arXiv:1504.02102 \[hep-ph\]](#).
- [10] Y. Ema, K. Nakayama, and Y. Tang, *JHEP* **07**, 060 (2019), [arXiv:1903.10973 \[hep-ph\]](#).
- [11] E. W. Kolb and A. J. Long, *JHEP* **03**, 283 (2021), [arXiv:2009.03828 \[astro-ph.CO\]](#).
- [12] B. Salehian, M. A. Gorji, H. Firouzjahi, and S. Mukohyama, *Phys. Rev. D* **103**, 063526 (2021), [arXiv:2010.04491 \[hep-ph\]](#).
- [13] A. Ahmed, B. Grzadkowski, and A. Socha, *JHEP* **08**, 059 (2020), [arXiv:2005.01766 \[hep-ph\]](#).
- [14] Y. Nakai, R. Namba, and Z. Wang, *JHEP* **12**, 170 (2020), [arXiv:2004.10743 \[hep-ph\]](#).
- [15] K. Nakayama and Y. Tang, *Phys. Lett. B* **811**, 135977 (2020), [arXiv:2006.13159 \[hep-ph\]](#).
- [16] H. Firouzjahi, M. A. Gorji, S. Mukohyama, and B. Salehian, *JHEP* **06**, 050 (2021), [arXiv:2011.06324 \[hep-ph\]](#).
- [17] M. Bastero-Gil, J. Santiago, L. Ubaldi, and R. Vega-Morales, *JCAP* **02**, 015 (2022), [arXiv:2103.12145 \[hep-ph\]](#).
- [18] H. Firouzjahi, M. A. Gorji, S. Mukohyama, and A. Talebian, *Phys. Rev. D* **105**, 043501 (2022), [arXiv:2110.09538 \[gr-qc\]](#).
- [19] T. Sato, F. Takahashi, and M. Yamada, (2022), [arXiv:2204.11896 \[hep-ph\]](#).
- [20] R. T. Co, A. Pierce, Z. Zhang, and Y. Zhao, *Phys. Rev. D* **99**, 075002 (2019), [arXiv:1810.07196 \[hep-ph\]](#).
- [21] J. A. Dror, K. Harigaya, and V. Narayan, (2018), [arXiv:1810.07195 \[hep-ph\]](#).
- [22] M. Bastero-Gil, J. Santiago, L. Ubaldi, and R. Vega-Morales, (2018), [arXiv:1810.07208 \[hep-ph\]](#).
- [23] P. Agrawal, N. Kitajima, M. Reece, T. Sekiguchi, and F. Takahashi, (2018), [arXiv:1810.07188 \[hep-ph\]](#).
- [24] R. T. Co, K. Harigaya, and A. Pierce, *JHEP* **12**, 099 (2021), [arXiv:2104.02077 \[hep-ph\]](#).
- [25] K. Nakayama and W. Yin, *JHEP* **10**, 026 (2021), [arXiv:2105.14549 \[hep-ph\]](#).
- [26] D. Cyncynates and Z. J. Weiner, (2023), [arXiv:2310.18397 \[hep-ph\]](#).
- [27] A. J. Long and L.-T. Wang, (2019), [arXiv:1901.03312 \[hep-ph\]](#).
- [28] A. E. Nelson and J. Scholtz, *Phys. Rev. D* **84**, 103501 (2011), [arXiv:1105.2812 \[hep-ph\]](#).
- [29] P. Arias, D. Cadamuro, M. Goodsell, J. Jaeckel, J. Redondo, and A. Ringwald, *JCAP* **06**, 013 (2012), [arXiv:1201.5902 \[hep-ph\]](#).
- [30] G. Alonso-Álvarez, T. Hugle, and J. Jaeckel, (2019), [arXiv:1905.09836 \[hep-ph\]](#).
- [31] K. Nakayama, *JCAP* **1910**, 019 (2019), [arXiv:1907.06243 \[hep-ph\]](#).
- [32] K. Nakayama, *JCAP* **08**, 033 (2020), [arXiv:2004.10036 \[hep-ph\]](#).
- [33] L. Hui, J. P. Ostriker, S. Tremaine, and E. Witten, *Phys. Rev. D* **95**, 043541 (2017), [arXiv:1610.08297 \[astro-ph.CO\]](#).
- [34] A. Suárez, V. H. Robles, and T. Matos, *Astrophys. Space Sci. Proc.* **38**, 107 (2014), [arXiv:1302.0903 \[astro-ph.CO\]](#).
- [35] L. A. Ureña-López, *Frontiers in Astronomy and Space Sciences* **6**, 47 (2019).
- [36] J. Suzuki, Y. Inoue, T. Horie, and M. Minowa, in *11th Patras Workshop on Axions, WIMPs and WISPs* (2015) pp. 145–148, [arXiv:1509.00785 \[hep-ex\]](#).
- [37] J. Suzuki, T. Horie, Y. Inoue, and M. Minowa, *JCAP* **09**, 042 (2015), [arXiv:1504.00118 \[hep-ex\]](#).
- [38] S. Knirck, T. Yamazaki, Y. Okesaku, S. Asai, T. Idehara, and T. Inada, *JCAP* **1811**, 031 (2018), [arXiv:1806.05120 \[hep-ex\]](#).
- [39] N. Tomita, S. Oguri, Y. Inoue, M. Minowa, T. Nagasaki, J. Suzuki, and O. Tajima, *JCAP* **09**, 012 (2020), [arXiv:2006.02828 \[hep-ex\]](#).
- [40] A. Andrianaivalomahefa *et al.* (FUNK Experiment), *Phys. Rev. D* **102**, 042001 (2020), [arXiv:2003.13144 \[astro-ph.CO\]](#).
- [41] A. Phipps *et al.*, *Springer Proc. Phys.* **245**, 139 (2020), [arXiv:1906.08814 \[astro-ph.CO\]](#).

- [42] B. Godfrey *et al.*, *Phys. Rev. D* **104**, 012013 (2021), [arXiv:2101.02805 \[physics.ins-det\]](#).
- [43] P. Brun, L. Chevalier, and C. Flouzat, *Phys. Rev. Lett.* **122**, 201801 (2019), [arXiv:1905.05579 \[hep-ex\]](#).
- [44] L. Hoang Nguyen, A. Lobanov, and D. Horns, *JCAP* **1910**, 014 (2019), [arXiv:1907.12449 \[hep-ex\]](#).
- [45] A. V. Dixit, S. Chakram, K. He, A. Agrawal, R. K. Naik, D. I. Schuster, and A. Chou, *Phys. Rev. Lett.* **126**, 141302 (2021), [arXiv:2008.12231 \[hep-ex\]](#).
- [46] S. De Panfilis, A. C. Melissinos, B. E. Moskowitz, J. T. Rogers, Y. K. Semertzidis, W. Wuensch, H. J. Halama, A. G. Prodel, W. B. Fowler, and F. A. Nezrick, *Phys. Rev. Lett.* **59**, 839 (1987).
- [47] C. Hagmann, P. Sikivie, N. S. Sullivan, and D. B. Tanner, *Phys. Rev.* **D42**, 1297 (1990).
- [48] G. B. Gelmini, A. J. Millar, V. Takhistov, and E. Vitagliano, *Phys. Rev. D* **102**, 043003 (2020), [arXiv:2006.06836 \[hep-ph\]](#).
- [49] A. Caputo, A. J. Millar, C. A. J. O'Hare, and E. Vitagliano, *Phys. Rev. D* **104**, 095029 (2021), [arXiv:2105.04565 \[hep-ph\]](#).
- [50] M. Lawson, A. J. Millar, M. Pancaldi, E. Vitagliano, and F. Wilczek, *Phys. Rev. Lett.* **123**, 141802 (2019), [arXiv:1904.11872 \[hep-ph\]](#).
- [51] S. R. Parker, J. G. Hartnett, R. G. Povey, and M. E. Tobar, *Phys. Rev. D* **88**, 112004 (2013), [arXiv:1410.5244 \[hep-ex\]](#).
- [52] S. Chaudhuri, P. W. Graham, K. Irwin, J. Mardon, S. Rajendran, and Y. Zhao, *Phys. Rev. D* **92**, 075012 (2015), [arXiv:1411.7382 \[hep-ph\]](#).
- [53] M. Silva-Feaver, S. Chaudhuri, H.-M. Cho, C. Dawson, P. Graham, K. Irwin, S. Kuenstner, D. Li, J. Mardon, H. Moseley, R. Mule, A. Phipps, S. Rajendran, Z. Steffen, and B. Young, *IEEE Transactions on Applied Superconductivity* **27**, 1 (2017).
- [54] S. Chaudhuri, K. Irwin, P. W. Graham, and J. Mardon, (2018), [arXiv:1803.01627 \[hep-ph\]](#).
- [55] A. Caldwell, G. Dvali, B. Majorovits, A. Millar, G. Raffelt, J. Redondo, O. Reimann, F. Simon, and F. Steffen (MADMAX Working Group), *Phys. Rev. Lett.* **118**, 091801 (2017), [arXiv:1611.05865 \[physics.ins-det\]](#).
- [56] S. D. McDermott and S. J. Witte, *Phys. Rev.* **D101**, 063030 (2020), [arXiv:1911.05086 \[hep-ph\]](#).
- [57] A. Caputo, H. Liu, S. Mishra-Sharma, and J. T. Ruderman, *Phys. Rev. Lett.* **125**, 221303 (2020), [arXiv:2002.05165 \[astro-ph.CO\]](#).
- [58] S. J. Witte, S. Rosauero-Alcaraz, S. D. McDermott, and V. Poulin, *JHEP* **06**, 132 (2020), [arXiv:2003.13698 \[astro-ph.CO\]](#).
- [59] H. An, F. P. Huang, J. Liu, and W. Xue, *Phys. Rev. Lett.* **126**, 181102 (2021), [arXiv:2010.15836 \[hep-ph\]](#).
- [60] H. An, X. Chen, S. Ge, J. Liu, and Y. Luo, *Nature Commun.* **15**, 915 (2024), [arXiv:2301.03622 \[hep-ph\]](#).
- [61] F. P. Kapron, D. B. Keck, and R. D. Maurer, *Appl. Phys. Lett.* **17**, 423 (1970).
- [62] T. Miya, Y. Terunuma, T. Hosaka, and T. Miyashita, *Electronics Letters* **15**, 106 (1979).
- [63] F. P. Kapron, R. D. Maurer, and M. P. Teter, *Appl. Opt.* **11**, 1352 (1972).
- [64] M. K. Barnoski and S. M. Jensen, *Appl. Opt.* **15**, 2112 (1976).
- [65] J. P. Dakin and B. Culsaw, *Optical Fiber Sensors: Principles and Components* (Artech House, 1988).
- [66] R. Hui and M. O'Sullivan, *FIBER-OPTIC MEASUREMENT TECHNIQUES* (Academic Press, 2023).
- [67] J. Senior, *Optical Fiber Communications: Principles and Practice* (Pearson, 2009).
- [68] K. Thyagarajan and A. Ghatak, *Lasers: Fundamentals and Applications* (Springer, 2011).

## Supplemental material: Dark Photon Oscillations in Waveguide

Yu-Xin Tian,<sup>1</sup> Wenyu Wang,<sup>1</sup> Wen-Na Yang,<sup>2</sup> Bin Zhu<sup>3</sup>

<sup>1</sup>*Beijing University of Technology, Beijing, China*

<sup>2</sup>*Department of Physics and Institute of Theoretical Physics, Nanjing Normal University, Nanjing, 210023, China*

<sup>3</sup>*School of Physics, Yantai University, Yantai 264005, China*

This section provides a step-by-step derivation that establishes the theoretical foundation for dark photon oscillation, detailing its mechanism, necessity, and how it guides the experimental probe.

### MAXWELL'S EQUATIONS AND PROPAGATION MODES IN A WAVEGUIDE

We start from Maxwell's equations in a uniform, lossless medium of permittivity  $\epsilon$  and permeability  $\mu$ , inside a hollow conducting waveguide. We assume time-harmonic fields  $\propto e^{-i\omega t}$ . Maxwell's curl equations give,

$$\nabla \times \mathbf{E} = i\omega \mathbf{B}, \quad \nabla \times \mathbf{B} = -i\mu\epsilon\omega \mathbf{E}, \quad \nabla \cdot \mathbf{E} = 0, \quad \nabla \cdot \mathbf{B} = 0.$$

We seek solutions propagating along the  $z$ -axis:

$$\mathbf{E}(x, y, z, t) = \mathbf{E}_t(x, y) e^{ik_z z - i\omega t}, \quad \mathbf{B}(x, y, z, t) = \mathbf{B}_t(x, y) e^{ik_z z - i\omega t}.$$

Substituting into Maxwell's equations yields the transverse Helmholtz equation:

$$[\nabla_t^2 + (\mu\epsilon\omega^2 - k_z^2)] \begin{pmatrix} \mathbf{E}_t \\ \mathbf{B}_t \end{pmatrix} = 0, \quad \nabla_t^2 \equiv \frac{\partial^2}{\partial x^2} + \frac{\partial^2}{\partial y^2}. \quad (\text{S.1})$$

By boundary conditions on the metallic walls (perfect conductor idealization first), only discrete transverse modes  $(\mathbf{E}_t, \mathbf{B}_t)$  satisfying appropriate vanishing tangential fields exist.

Eq. (S.1) identifies allowed transverse mode functions and defines a cutoff condition. Each mode behaves as if the photon has an effective ‘‘mass’’  $m_\xi$  given by its cutoff frequency. For each mode label  $\xi$ , the transverse eigenvalue equation yields

$$\nabla_t^2 \psi_\xi + \mu\epsilon\omega_\xi^2 \psi_\xi = 0, \quad (\text{S.2})$$

with cutoff frequency  $\omega_\xi$  determined by geometry (e.g., for rectangular waveguide TE $_{mn}$  mode,  $\omega_{mn}^2 = \pi^2(\frac{m^2}{a^2} + \frac{n^2}{b^2})/(\mu\epsilon)$ ). Define effective mass  $m_\xi \equiv \omega_\xi$ , then propagation along  $z$  obeys

$$k_z^2 = \omega^2 - m_\xi^2. \quad (\text{S.3})$$

Hence, the wave equation for the field envelope along  $z$  is analogous to a Klein–Gordon equation,

$$[-\partial_t^2 + \partial_z^2 - m_\xi^2] \psi = 0. \quad (\text{S.4})$$

Phase and group velocities follow

$$v_{p,\xi} = \frac{\omega}{k_z} = \frac{\omega}{\sqrt{\omega^2 - m_\xi^2}}, \quad v_{g,\xi} = \frac{d\omega}{dk_z} = \sqrt{1 - \frac{m_\xi^2}{\omega^2}}, \quad v_{p,\xi} v_{g,\xi} = 1. \quad (\text{S.5})$$

Viewing each mode as a ‘‘massive photon’’ clarifies how a dark photon of mass  $m_{A'}$  can resonantly mix when  $m_{A'} \approx m_\xi$ . We briefly recall the separation into TE and TM modes:

- **TE modes:**  $E_z = 0$ , nonzero  $B_z$ , with boundary condition  $\partial_n B_z|_{\text{wall}} = 0$ .
- **TM modes:**  $B_z = 0$ , nonzero  $E_z$ , with  $E_z|_{\text{wall}} = 0$ .

For a rectangular waveguide of cross-section  $a \times b$ , the standard solutions have

$$\psi_{mn}(x, y) = \cos\left(\frac{m\pi x}{a}\right) \cos\left(\frac{n\pi y}{b}\right) \quad \text{or} \quad \sin\left(\frac{m\pi x}{a}\right) \sin\left(\frac{n\pi y}{b}\right), \quad (\text{S.6})$$

leading to cutoff  $\omega_{mn}^2 = \pi^2(\frac{m^2}{a^2} + \frac{n^2}{b^2})/(\mu\epsilon)$ . Explicit mode functions allow computing normalization integrals (power, energy) below. The time-averaged axial power flow in mode  $\xi$  is

$$P(z) = \int_{A_{\text{cross}}} \Re[\frac{1}{2}\mathbf{E} \times \mathbf{H}^*] \cdot \hat{\mathbf{z}} dA. \quad (\text{S.7})$$

Using mode functions, one shows

$$P = \frac{1}{2\sqrt{\mu\epsilon}} \frac{\omega^2}{\omega_\xi^2} \sqrt{1 - \frac{\omega_\xi^2}{\omega^2}} \kappa_\xi \int_A |\psi_\xi|^2 dA, \quad (\text{S.8})$$

where  $\kappa_\xi = \epsilon$  for TM modes or  $\mu$  for TE modes. The ratio of power to stored energy  $U$  yields group velocity  $v_{g,\xi}$ :

$$\frac{P}{U} = v_{g,\xi}, \quad U = \frac{1}{2} \int_A (\epsilon|\mathbf{E}|^2 + \mu|\mathbf{H}|^2) dA. \quad (\text{S.9})$$

With finite wall conductivity,  $k_z$  acquires a small imaginary part:

$$k_z \simeq k_z^{(0)} + \varepsilon_\xi + i\beta_\xi,$$

where  $\beta_\xi > 0$  causes decay. The power decays as

$$P(z) = P_0 e^{-2\beta_\xi z}, \quad \beta_\xi = -\frac{1}{2P} \frac{dP}{dz} \Big|_{\text{ohmic}}. \quad (\text{S.10})$$

We assume  $\beta_\xi$  known (measured or from theory) and will later normalize by  $e^{2\beta_\xi z}$ . Experimentally, one must correct for ordinary loss to isolate oscillation.

## THE PROPAGATION AND OSCILLATION OF DARK PHOTONS

Introduce a dark U(1) gauge field  $A'_\mu$  with mass  $m_{A'}$ , kinetically mixed with the visible photon  $A_\mu$  via small parameter  $\varepsilon$ . After field redefinitions, the relevant quadratic Lagrangian in interaction basis  $(A, A')$  can be written (in Lorenz gauge) as

$$\mathcal{L} \supset -\frac{1}{4}F_{\mu\nu}F^{\mu\nu} - \frac{1}{4}F'_{\mu\nu}F'^{\mu\nu} - \frac{1}{2}m_{A'}^2 A'_\mu A'^\mu - \frac{1}{2}\varepsilon F_{\mu\nu}F'^{\mu\nu}.$$

In the waveguide, the visible field  $A$  obeys the massive dispersion due to mode cutoff: effectively  $m_\xi^2$  enters. The dark field  $A'$  is not confined transversely, so it propagates as a plane wave in  $z$ . The coupled wave equation along  $z$  for the two fields (suppressing polarization indices, focusing on one polarization/mode) becomes:

$$\left[ -\partial_t^2 + \partial_z^2 - \begin{pmatrix} m_\xi^2 & -\varepsilon m_{A'}^2 \\ -\varepsilon m_{A'}^2 & m_{A'}^2 \end{pmatrix} \right] \begin{pmatrix} A(z, t) \\ A'(z, t) \end{pmatrix} = 0. \quad (\text{S.11})$$

Here  $A(z, t) = A(x, y) e^{i(k_z z - \omega t)}$  with transverse profile  $A(x, y)$  normalized to the chosen mode, giving  $-\partial_t^2 + \partial_z^2 + \partial_x^2 + \partial_y^2 \rightarrow -\partial_t^2 + \partial_z^2 - m_\xi^2$  on  $A$ . For  $A'$ , transverse Laplacian is zero, giving  $-\partial_t^2 + \partial_z^2 - 0$ ; but mixing induces off-diagonal  $-\varepsilon m_{A'}^2$  and diagonal  $m_{A'}^2$  terms after field redefinition. Eq. (S.11) encapsulates how the effective masses and mixing produce two coupled modes that will split into two propagation eigenstates.

Assume harmonic time dependence  $e^{-i\omega t}$  and spatial dependence  $e^{ik_z z}$ . Insert

$$A(z, t) = A_0 e^{ik_z z - i\omega t}, \quad A'(z, t) = A'_0 e^{ik_z z - i\omega t}. \quad (\text{S.12})$$

Equation (S.11) becomes an algebraic condition on  $k_z$  and amplitudes:

$$[\omega^2 - k_z^2] \begin{pmatrix} A_0 \\ A'_0 \end{pmatrix} = \begin{pmatrix} m_\xi^2 & -\varepsilon m_{A'}^2 \\ -\varepsilon m_{A'}^2 & m_{A'}^2 \end{pmatrix} \begin{pmatrix} A_0 \\ A'_0 \end{pmatrix}. \quad (\text{S.13})$$

Rearrange to

$$k_z^2 = \omega^2 - M^2, \quad \text{with} \quad M^2 \equiv \begin{pmatrix} m_\xi^2 & -\varepsilon m_{A'}^2 \\ -\varepsilon m_{A'}^2 & m_{A'}^2 \end{pmatrix}. \quad (\text{S.14})$$

Thus the eigenvalues  $m_{B_1}^2, m_{B_2}^2$  of  $M^2$  determine the two propagation constants:

$$k_{z,B_i} = \sqrt{\omega^2 - m_{B_i}^2}, \quad i = 1, 2. \quad (\text{S.15})$$

Diagonalize  $M^2$  by orthogonal rotation:

$$\begin{pmatrix} B_1 \\ B_2 \end{pmatrix} = \begin{pmatrix} \cos \theta & -\sin \theta \\ \sin \theta & \cos \theta \end{pmatrix} \begin{pmatrix} A \\ A' \end{pmatrix}. \quad (\text{S.16})$$

The mixing angle  $\theta$  satisfies

$$\tan 2\theta = \frac{2\varepsilon m_{A'}^2}{m_{A'}^2 - m_\xi^2}. \quad (\text{S.17})$$

Eigenvalues are

$$m_{B_{1,2}}^2 = \frac{m_\xi^2 + m_{A'}^2 \pm \sqrt{(m_\xi^2 - m_{A'}^2)^2 + 4\varepsilon^2 m_{A'}^4}}{2}. \quad (\text{S.18})$$

When  $m_\xi^2 \approx m_{A'}^2$  and  $\varepsilon \ll 1$ , expand:

$$m_{B_{1,2}}^2 \simeq \frac{m^2 + m^2 \pm 2\varepsilon m^2}{2} = m^2 \pm \varepsilon m^2, \quad m \equiv m_\xi \approx m_{A'}. \quad (\text{S.19})$$

Thus splitting  $\Delta m^2 \sim 2\varepsilon m^2$ . Corresponding  $k_{z,B_i} \approx \sqrt{\omega^2 - m^2 \mp \varepsilon m^2}$ . Diagonalization identifies two propagation eigenstates  $B_1, B_2$  with slightly different effective masses and hence different  $k_z$  and velocities. The small mixing  $\varepsilon$  introduces the splitting needed for interference.

We prepare a pure visible photon state at the waveguide input ( $z = 0$ ):  $A'(0) = 0$ . Using Eq. (S.16), express initial amplitudes in eigenbasis:

$$A(0) = A_0, \quad A'(0) = 0 \quad \Rightarrow \quad \begin{cases} B_1(0) = \cos \theta A_0, \\ B_2(0) = \sin \theta A_0, \end{cases} \quad \text{so } B_2(0)/B_1(0) = \tan \theta. \quad (\text{S.20})$$

Each eigenstate then propagates as

$$B_i(z, t) = B_i(0) e^{i(k_{z,B_i} z - \omega t)}. \quad (\text{S.21})$$

Hence the visible field at  $(z, t)$  is

$$A(z, t) = \cos \theta B_1(0) e^{i(k_{z,B_1} z - \omega t)} + \sin \theta B_2(0) e^{i(k_{z,B_2} z - \omega t)}. \quad (\text{S.22})$$

The decomposition shows that the visible field is a superposition of two eigenmodes accumulating different phases  $\propto k_{z,B_i} z$ , leading to interference.

Compute axial Poynting flux  $S_z \propto \Re[E \times H^*] \cdot \hat{z}$ . Since fields carry factors from Eq. (S.22), the power density contains terms  $\propto |A(z, t)|^2$ . After integrating over cross-section, one obtains:

$$P(z) = P_0 e^{-2\beta_\xi z} \left[ \eta_1^2 + \eta_2^2 + 2\eta_1\eta_2 \cos((k_{z,B_1} - k_{z,B_2})z) \right]. \quad (\text{S.23})$$

Here  $\eta_1 = \cos \theta$ ,  $\eta_2 = \sin \theta$  up to normalization. The factor  $e^{-2\beta_\xi z}$  accounts for ordinary attenuation (assumed similar for both eigenmodes).  $\Delta k_z = k_{z,B_1} - k_{z,B_2}$ .

At exact resonance ( $m_\xi = m_{A'}$ ),  $\theta = \pi/4$ , so  $\eta_1 = \eta_2 = 1/\sqrt{2}$  and

$$P(z) = P_0 e^{-2\beta_\xi z} \left[ \frac{1}{2} + \frac{1}{2} \cos(\Delta k_z z) \right]. \quad (\text{S.24})$$

This shows explicitly that power oscillates with spatial period  $\lambda_{\text{osc}} = 2\pi/\Delta k_z$  on top of exponential decay. Detecting the cosine modulation is the objective.

## THE FOURIER ANALYSIS OF PULSED SIGNALS AND DATA PROCESSING FOR MEASUREMENT

We choose a periodic square pulse train for OTDR detection, because OTDR uses pulses to locate scattering at different  $z$ . Let the input temporal waveform shown in the panel c) of Fig. 2 be

$$f(0, t) = A(t) \sin(\omega_0 t), \quad A(t) = \text{sign}(\text{mod}(t, \tau) - \frac{\tau}{2}),$$

with carrier frequency  $\omega_0$  and pulse period  $2\tau$  (modulation frequency  $\Omega = \pi/\tau$ ,  $\Omega \ll \omega_0$ ). Express  $f(0, t)$  as,

$$f(0, t) \simeq \frac{A_0}{2} \sin(\omega_0 t) + \sum_{n=1}^{N_{\text{max}}} C_n \sin((\omega_0 - n\Omega)t) + \sum_{n=1}^{\infty} C_n \sin((\omega_0 + n\Omega)t), \quad (\text{S.25})$$

where

$$C_n = \frac{A_0}{n\pi} \sin\left(\frac{n\pi}{2}\right), \quad N_{\text{max}} \approx \lfloor \omega_0/\Omega \rfloor. \quad (\text{S.26})$$

The second sum covers lower sidebands, the third covers higher. Decomposing into sinusoidal components allows analyzing each frequency's propagation and interference separately.

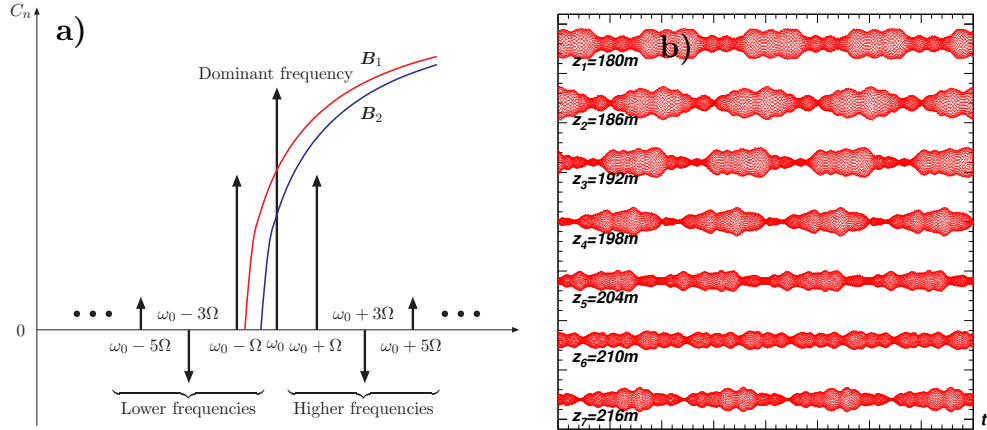


Figure S1. The sketch map of the oscillation phenomenon in the optical fiber. a) The component frequency of the periodic square pulse and the resonant mode. The red and blue curve show the group velocity of the two resonant modes; b) The numerical simulated periodic "D+H" square pulse at different sample positions.

When  $\omega_0$  is tuned close to the cutoff  $\omega_\xi \approx m_{A'}$ , any component with frequency  $\omega < \omega_\xi$  becomes evanescent: its  $k_z$  is imaginary, leading to rapid exponential decay over a short distance. Thus, for distances beyond a small region, only components with  $\omega \geq \omega_\xi$  survive. Since  $\omega_0 \approx \omega_\xi$ , the lower sidebands ( $\omega_0 - n\Omega$ ) fall below cutoff and die out; only the dominant tone  $\omega_0$  and higher sidebands ( $\omega_0 + n\Omega$ ) propagate, as shown in the Fig. S1. We denote this filtered input as

$$f^{\text{D+H}}(0, t) = \frac{A_0}{2} \sin(\omega_0 t) + \sum_{n=1}^{\infty} C_n \sin((\omega_0 + n\Omega)t). \quad (\text{S.27})$$

Filtering simplifies analysis: we only track frequencies above cutoff, which propagate and exhibit oscillation.

For each surviving component frequency  $\omega_n = \omega_0 + n\Omega$ , the two eigenmodes have propagation constants:

$$k_{z,B_i}^{(n)} = \sqrt{\omega_n^2 - m_{B_i}^2}, \quad i = 1, 2. \quad (\text{S.28})$$

Group and phase velocities differ slightly due to  $m_{B_i}$  splitting. After traveling distance  $L$ , the relative phase between eigenmodes for component  $n$  is:

$$\Delta\varphi_n = L \left[ \sqrt{(\omega_0 + n\Omega)^2 - m_{B_1}^2} - \sqrt{(\omega_0 + n\Omega)^2 - m_{B_2}^2} \right]. \quad (\text{S.29})$$

For small mixing ( $\varepsilon \ll 1$ ) and near resonance ( $\omega_0 \approx m_{B_2} \approx m_{A'}$ ), expand

$$m_{B_{1,2}}^2 \approx m^2 \pm \varepsilon m^2, \quad m \equiv m_{A'}, \quad (\text{S.30})$$

so for  $\omega_n \sim m$ ,

$$\sqrt{\omega_n^2 - (m^2 \pm \varepsilon m^2)} \approx \sqrt{\omega_n^2 - m^2} \mp \frac{\varepsilon m^2}{2\sqrt{\omega_n^2 - m^2}}. \quad (\text{S.31})$$

Thus their difference

$$\Delta\varphi_n \approx L \frac{\varepsilon m^2}{\sqrt{\omega_n^2 - m^2}} \approx L \frac{\varepsilon m^2}{k_z^{(0)}}, \quad (\text{S.32})$$

where  $k_z^{(0)} = \sqrt{\omega_n^2 - m^2}$ . At exact resonance  $\omega_n \approx m$ ,  $k_z^{(0)}$  small, but more careful treatment shows leading scaling

$$\Delta\varphi_0 \sim \sqrt{2\varepsilon} mL. \quad (\text{S.33})$$

as derived from full expression under  $m_{B_{1,2}}^2 = m^2(1 \pm \varepsilon)$ .

Computing  $\Delta\varphi_n$  quantifies the interference period  $\lambda_{\text{osc}} = 2\pi/\Delta k_z$  and amplitude of oscillation for each harmonic. At position  $z$ , the total field is the sum of harmonics and eigenmodes:

$$f^{\text{D+H}}(z, t) = \sum_{n=0}^{\infty} \left[ \eta_1 C'_n \sin(\omega_n t - k_{z,B_1}^{(n)} z) + \eta_2 C'_n \sin(\omega_n t - k_{z,B_2}^{(n)} z) \right], \quad (\text{S.34})$$

where  $C'_0 = A_0/2$  for  $n = 0$  and  $C'_n = C_n$  for  $n \geq 1$ . The measured power (time-averaged) depends on interference term  $\cos \left[ (k_{z,B_1}^{(n)} - k_{z,B_2}^{(n)}) z \right] = \cos(\Delta\varphi_n)$ . Summing contributions effectively yields a modulation in the envelope of the pulse's amplitude vs.  $z$ . This illustrates how the waveform distortion emerges from different phase velocities, and more importantly, how the power oscillates. Right panel of Fig. S1 shows the simulated waveform of the D+H tune at different sample positions.

A real laser has linewidth: model each frequency component with Lorentzian distribution centered at  $\omega_c$ :

$$g(\omega, \omega_c) = \frac{1}{\pi} \frac{\Gamma^2}{(\omega - \omega_c)^2 + \Gamma^2}, \quad \Gamma = \frac{\omega_c \zeta}{2}, \quad \zeta = \frac{\Delta\nu}{\nu}. \quad (\text{S.35})$$

Here  $\zeta \sim 10^{-5}$  (ordinary) or  $\zeta \sim 10^{-11}$  (ultra-stable). We average the phase difference for the dominant frequency component around  $\omega_c \approx m_{B_2}$

$$\begin{aligned} \overline{\Delta\varphi_0} &= \frac{1}{\Gamma} \int_{m_{B_2}}^{\infty} \left[ \sqrt{\omega^2 - (m_{B_2}^2 - 2\varepsilon m_{A'}^2)} - \sqrt{\omega^2 - m_{B_2}^2} \right] g(\omega, m_{B_2}) d\omega. \\ &= \frac{4\varepsilon L}{\lambda} \int_0^{\infty} \frac{1}{\sqrt{x\zeta + 2\varepsilon} + \sqrt{x\zeta}} \frac{1}{1+x^2} dx. \end{aligned} \quad (\text{S.36})$$

Change variables and approximate for  $\zeta \ll \varepsilon$ , We can see that  $\overline{\Delta\varphi_0}$  returns to Eq. (S.36)

$$\overline{\Delta\varphi_0} \approx \sqrt{2\varepsilon} m_{A'} L, \quad (\text{S.37})$$

showing that finite linewidth reduces coherence only if  $\zeta \gtrsim \varepsilon$ . If  $\zeta \gg \varepsilon$ , oscillation averages out.

Incorporating laser linewidth shows realistic sensitivity limits. It justifies using long-coherence lasers to probe smaller  $\varepsilon$ . Set the minimal detectable phase difference  $\Delta\varphi_0 \approx 2\pi$  over fiber length  $L$ . Using  $\Delta\varphi_0 \approx \sqrt{2\varepsilon} m_{A'} L$ , solve:

$$\varepsilon \approx \frac{1}{2} \left( \frac{2\pi}{m_{A'} L} \right)^2. \quad (\text{S.38})$$

Equivalently,

$$\log_{10} \varepsilon \approx 2 \log_{10} \left( \frac{2\pi}{m_{A'} L} \right) - \log_{10} 2. \quad (\text{S.39})$$

In terms of wavelength  $\lambda = 2\pi/m_{A'}$ ,  $L/\lambda$  enters. For  $L = 10^6$  m,  $\lambda = 10^{-6}$  m, one gets  $\varepsilon \sim 10^{-24}$ . Provides target coupling sensitivity; shows advantage of long baseline and resonant enhancement ( $\sqrt{\varepsilon}$  scaling). Using averaged phase from Eq. (S.36), require  $\overline{\Delta\varphi_0} \sim 0.01 \times 2\pi$  to solve for  $\varepsilon$  given  $\zeta$  and  $L$ . Plotting  $\varepsilon$  vs.  $m_{A'}$  yields exclusion reach (as in Fig. 3).

Generally speaking, the experimental measurements of the oscillation is simple. Both power flow which is measured by a power meter, and the amplitude which is shown by the oscilloscope, can be chosen for the display in the panel a) of Fig. 2. Suppose the power flow are measured at a series of lengths for the prepared fiber with a radius  $r_i$

$$\mathcal{M} = [\hat{P}(z_1; r_i), \hat{P}(z_2; r_i), \dots, \hat{P}(z_n; r_i)]. \quad (\text{S.40})$$

Then, every sample measurement should be normalized by the attenuation factor  $\beta_\xi$

$$\mathcal{E} = [\hat{P}(z_1; r_i)e^{2\beta_\xi z_1}, \hat{P}(z_2; r_i)e^{2\beta_\xi z_2}, \dots, \hat{P}(z_n; r_i)e^{2\beta_\xi z_n}] = [P(z_1; r_i), P(z_2; r_i), \dots, P(z_n; r_i)]. \quad (\text{S.41})$$

Taking the data set  $\mathcal{E}$  to fit the cosine function along the  $z$  will be the evidence of the oscillation.

In addition to the monochromaticity of the laser, there are many other different kinds of noise and disturbance, such the noise from the equipments, thermal environment, and the error of the attenuation factor, etc. These disturbances are rather difficult for a precision measurements. Anyway, a more precise fit for the cosine wave is in the data processing, especially in case of that the oscillation wavelength is much larger than the fiber length. Suppose the variation of the normalized power flow is rather small, slightly oscillates along with the propagation distance. Then the phase difference can be extracted by the asymptotic Taylor expansion of the cosine function. For example, the power flow are measured at the input end and the tail end, giving the measured power flow  $P(0)$ ,  $P(L)$ . Then, expanding the Eq. (S.23) together with the noise  $P_N$

$$P(0; r_i) = P_0(\eta_1^2 + \eta_2^2 + 2\eta_1\eta_2) + P_N \quad (\text{S.42})$$

$$P(L; r_i) \simeq P_0 \left[ \eta_1^2 + \eta_2^2 + 2\eta_1\eta_2 \left( 1 - \frac{1}{2}(\Delta k_z L)^2 + \frac{1}{24}(\Delta k_z L)^4 \right) \right] + P_N. \quad (\text{S.43})$$

Here  $P_N$  roughly accounts for all the noises caused by the equipments, thermal environment, and the attenuation factor talked above. Generally  $P_N$  is kind of the resolution of the measurements which should be independent for the propagation length  $L$ . And it is rather tiny compared the input power flow  $P_0$ . For the slightly oscillation, we'd better define a linear relation

$$M(L; r_i) = \frac{P(L; r_i)}{P(0; r_i)} \simeq 1 - C_1 L^2 + C_2, \quad (\text{S.44})$$

in which

$$C_1 = \frac{\eta_1\eta_2}{(\eta_1 + \eta_2)^2} (\Delta k_z)^2, \quad C_2 = \frac{P_N}{P(0; r_i)}, \quad (\text{S.45})$$

for the numerical simulation of the data. A non-zero  $C_1$  serve as the criteria for oscillation detection, and the for the resonant mode with corresponding radius  $r_i$  gives us further information of the dark photon. Then the  $\chi^2$  is defined as

$$\chi^2 = \sum_n^N [M(L_n; r_i) - 1 + C_1 L_n^2 - C_2]^2. \quad (\text{S.46})$$

The Least Squared Method gives the best matching result

$$C_1 = \frac{\left(\sum_n^N L_n^2\right) \left(\sum_n^N M(L_n; r_i)\right) - N \left(\sum_n^N [M(L_n; r_i) L_n^2]\right)}{N \left(\sum_n^N L_n^4\right) - \left(\sum_n^N L_n^2\right)^2}, \quad (\text{S.47})$$

$$C_2 = \frac{\left(\sum_n^N L_n^4\right) \left(\sum_n^N M(L_n; r_i)\right) - \sum_n^N [M(L_n; r_i) L_n^2] \left(\sum_n^N M(L_n; r_i)\right)}{N \left(\sum_n^N L_n^4\right) - \left(\sum_n^N L_n^2\right)^2} - 1. \quad (\text{S.48})$$

As talked above, the optical fiber are prepared with an increasing radii. Only the one near the resonant mode (with a radius  $r_r$ ) can give significant non-zero  $C_1$ . Then more precise measurements should be taken around the corresponding radius  $r_r$ .

Then one may worry about that the mixing parameters  $\eta_1, \eta_2$  are unknown, This can be easily steered clear of by analyzing the power flow at two different points, say  $z = L/2, L$ . The phase difference can be easily derived form the expansion Eq. (S.43), and we can define a measurable quantity  $\mathcal{E}(L; r_r)$

$$\mathcal{E}(L; r_r) = \frac{P(L/2; r_r) - P(0; r_r)}{P(L; r_r) - P(0; r_r)} \simeq \frac{1}{4} \left[ 1 + \frac{1}{16} (\Delta k_z L)^2 \right]. \quad (\text{S.49})$$

Take  $\Delta k_z L = 0.01 \times 2\pi$  for the demonstration, then the measured  $(\mathcal{E} - 0.25) \times 100 \simeq 0.006$ . A much more precise  $\Delta k_z L$  can be extracted by this relation if the oscillation wavelength  $\lambda_{\text{osc}}$  is too much long. Three measured samples are enough for the fitting for the oscillation.